The effect of water on strain localization in calcite fault gouge sheared at seismic slip rates

Marieke Rempe, Steven Smith, Thomas Mitchell, Takehiro Hirose, Giulio Di Toro

PII: S0191-8141(17)30044-5

DOI: 10.1016/j.jsg.2017.02.007

Reference: SG 3449

To appear in: *Journal of Structural Geology*

Received Date: 22 July 2016

Revised Date: 8 February 2017

Accepted Date: 18 February 2017

Please cite this article as: Rempe, M., Smith, S., Mitchell, T., Hirose, T., Di Toro, G., The effect of water on strain localization in calcite fault gouge sheared at seismic slip rates, *Journal of Structural Geology* (2017), doi: 10.1016/j.jsg.2017.02.007.

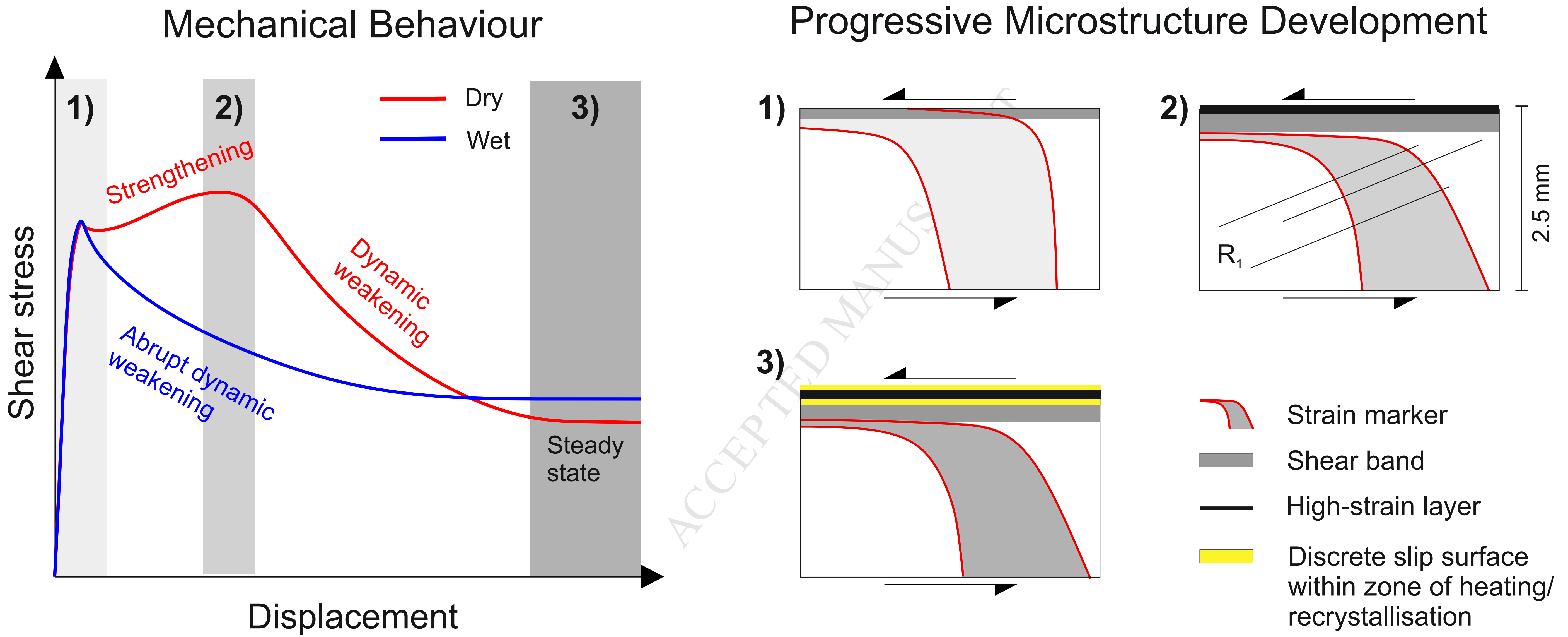
Mechanical Behaviour
Progressive Microstructure Development
1)
2)
3)
Dry
Wet
Strengthening
Dynamic weakening
Abrupt dynamic weakening
Steady state
Shear stress
Displacement
1)
2)
3)
R$_1$
2.5 mm
Strain marker
Shear band
High-strain layer
Discrete slip surface within zone of heating/ recrystallisation

The effect of water on strain localization in calcite fault gouge sheared at seismic slip rates

Marieke Rempe[1,2,*], Steven Smith[3], Thomas Mitchell[4], Takehiro Hirose[5], Giulio DI TORO[1,6,7]

*Corresponding Author

[1]Università degli Studi di Padova
Dipartimento di Geoscienze
Via G. Gradenigo, 6
35131 Padova, PD
Italy

[2]now at: Ruhr-Universitaet Bochum
Institute of Geology, Mineralogy and Geophysics
Universtitaetsstr. 150
44801 Bochum
Germany
marieke.rempe@rub.de
+49 (0)234 32-23272

[3]University of Otago
Department of Geology
Dunedin 9054
New Zealand
steven.smith@otago.ac.nz

[4]University College London
Rock & Ice Physics Laboratory and UCL SeismoLab
Department of Earth Sciences
London, WC1E 6BT
UK
tom.mitchell@ucl.ac.uk

[5]Kochi Institute for Core Sample Research, JAMSTEC,
200 Monobe Otsu, Nankoku-shi, Kochi, 783-8502,
Japan
hiroset@jamstec.co.jp

[6]University of Manchester
School of Earth, Atmospheric & Environmental Sciences
Oxford Road
Manchester M13 9PL

UK
giulio.ditoro@manchester.ac.uk

[7]Istituto Nazionale di Geofisica e Vulcanologia (INGV)
Via di Vigna Murata 655
Rome
Italy

Keywords

Fault gouge; localization; calcite; rotary-shear experiments; earthquakes; dynamic weakening

Abstract

Strain localization during coseismic slip in fault gouges is a critical mechanical process that has implications for understanding frictional heating, the earthquake energy budget and the evolution of fault rock microstructure. To assess the nature of strain localization during shearing of calcite fault gouges, high-velocity ($v_{\max} = 1\ \mathrm{m/s}$) rotary-shear experiments at normal stresses of 3–20 MPa were conducted under room-dry and wet conditions on synthetic calcite gouges containing dolomite gouge strain markers. When sheared at 1 m/s, the room-dry gouges showed a prolonged strengthening phase prior to dynamic weakening, whereas the wet gouges weakened nearly instantaneously. Microstructural analysis revealed that a thin (<600 µm) high-strain layer and through-going principal slip surface (PSS) developed after several centimeters of slip in both dry and wet gouges, and that strain localization at 1 m/s occurred progressively and rapidly. The strain accommodated in the bulk gouge layer did not change significantly with increasing displacement indicating that, once formed, the high-strain layer and PSS accommodated most of the displacement. Thus, a substantial strain gradient is present in the gouge layer. In water-dampened gouges, localization likely occurs during and after dynamic weakening. Our results suggest that natural fault zones in limestone are more prone to rapid dynamic weakening if water is present in the granular slipping zones.

1. Introduction

Field and trench observations from large fault zones show that while the surface trace of a fault can have a complex and broadly distributed geometry (Rockwell and Ben-Zion, 2007), co-seismic slip at depth is often localized within subcentimeter-thick gouge- and cataclasite-bearing principal slip zones (Sibson, 2003). There is also evidence that within these principal slip zones, localization to the sub mm-scale takes place during individual coseismic slip events (e.g., Chester et al., 1993; Chester and Chester, 1998; Boullier et al., 2009; Fondriest et al., 2012; Fondriest et al., 2013; Siman-Tov et al., 2013; Smith et al., 2013), although distributed coseismic deformation also occurs, e.g. at fault irregularities (Sibson, 1986; Pavlis et al., 1993; Aben et al., 2016).

The degree of strain localization and the thickness of the active principal slip zone strongly influence the dynamic behavior of faults (Ben-Zion and Sammis, 2003; Heermance et al., 2003; Rockwell and Ben-Zion, 2007), including the production of frictional heat and the evolution of thermally-sensitive weakening mechanisms. For example, Platt et al. (2014) modeled the shear strength evolution of a fluid-saturated gouge layer sheared at seismic slip rates (1 m/s), taking into consideration the role of thermally-driven weakening mechanisms. They found that during the early stages of deformation the shear strength evolution is similar to that modeled for uniform shearing (Rempel and Rice, 2006), but the onset of strain localization is accompanied by an acceleration in dynamic weakening because localization focuses frictional heating into a thinner zone, and consequently thermal pressurization becomes more effective (Lachenbruch, 1980).

In high-velocity experimental studies on gouge layers, shear localizes to a thin (<300 μm) and highly-comminuted slip zone cut by one or more discrete slip surfaces (Han et al., 2010;

Kitajima et al., 2010; De Paola et al., 2011; Fondriest et al., 2013; Smith et al., 2015). Evidence of intense strain localization and frictional heating is preserved as zones containing gouge material that is ultracomminuted, decomposed, recrystallized or sintered (e.g., Sawai et al., 2012; Togo and Shimamoto, 2012; Smith et al., 2013; Yao et al., 2013). The observed dynamic weakening that accompanies strain localization has been attributed to flash heating in a thin (≤30 μm) layer of wear material (Goldsby and Tullis, 2011; Kohli et al., 2011) or rapid diffusional processes in nanograins accompanying superplastic behavior (Verberne et al., 2013; Verberne et al., 2014b; De Paola et al., 2015; Green et al., 2015). In the case of carbonate rocks, flash weakening could be enhanced by decarbonation due to frictional heating and formation of CaO nanograins (Han et al., 2007; Han et al., 2010; Violay et al., 2014). The formation of nanograin material may be responsible for the velocity-weakening behavior of carbonate gouges sheared at low velocity (~1 μm) and elevated temperatures of 80–100 °C (Verberne et al., 2010; Verberne et al., 2014a; Verberne et al., 2014b) as well as for the low steady-state shear stress at high velocity (c. 1 m/s; De Paola et al., 2015; Green et al., 2015) due to enhancement of grain boundary sliding mechanisms.

Results from high-velocity experiments on room-dry calcite (Smith et al., 2015) and serpentinite (Proctor et al., 2014) gouges showed that strain was localized to a high-strain shear band prior to dynamic weakening, consistent with the idea that extreme localization in gouges is a necessary precursor to dynamic weakening (Goldsby and Tullis, 2011). However, the effect of water on localization and dynamic strength evolution in carbonate gouges has not yet been studied. This is important because field studies of natural slip zones in carbonates have shown that localized slip is commonly associated with the formation of veins and microstructures that indicate gouge fluidization (Smith et al., 2011; De Paola et al., 2012; Fondriest et al., 2012; Rowe et al., 2012), suggesting that in many carbonate-bearing fault zones coseismic slip occurs in the presence of hydrous fluids. The presence of water was found to significantly decrease the strength of clay-bearing gouges sheared at low to high velocities (Morrow et al., 2000; Kitajima et al., 2010; Ujiie and Tsutsumi, 2010; Faulkner et al., 2011; Han and Hirose, 2012; Verberne et al., 2014a; Bullock et al., 2015). The aim of this experimental study was to understand the strain-localization process in wet calcite gouges. To this end, we conducted rotary-shear experiments over a wide range of total displacements on dry and wet calcite gouges including the systematic use of strain markers.

2. Material and Methods

Two different rotary shear apparatus were used in this study: the Slow-to High Velocity Apparatus (SHIVA; Di Toro et al. (2010)) installed at the Istituto Nazionale di Geofisica e Vulcanologia in Rome, Italy, and the Pressurized High-Velocity apparatus (Phv) installed at the Kochi Institute for Core Sample Research/JAMSTEC in Nankoku, Japan (Tadai et al., 2009; Tanikawa et al., 2012). The gouge holder used in conjunction with SHIVA allowed us to easily construct a strain marker within the gouge layers, but pore-fluid conditions could not be controlled. Experiments under controlled pore-fluid conditions were performed using the Phv apparatus, which is equipped with a servo-controlled pore-fluid pressure system. Using the two different apparatus provides the additional advantage of being able to test the reproducibility of the mechanical data.

2.1. Experimental Set-Up of the SHIVA apparatus

A total of 18 high-velocity, rotary-shear experiments were performed with SHIVA using strain markers (Table 1). The gouge experiments were performed at a target maximum slip rate of 1 m/s, acceleration and deceleration of 6 m/s^2, normal stresses ranging from 3–20 MPa, total displacements from 0.011–2.5 m, and under room-dry or water-dampened conditions (Table 1). The design and capability of SHIVA are described in Di Toro et al. (2010) and Niemeijer et al. (2011). The annular gouge holder used with SHIVA (description and calibration tests in Smith et al., 2013) is built mainly from steel. The gouge layer has inner and outer diameters of 35 and 55 mm and is contained above and below by base discs and to the sides by steel rings that slide over the upper base disc (Fig. 1a). As the confining rings are in contact with the base discs, but are not designed to carry load, springs located underneath the rings ensure that the normal load is mainly supported by the gouge layer (Smith et al., 2013). To minimize the contribution of the sliding rings to the measured torque, the contact area of the rings with the base disc was lubricated with high-temperature grease prior to each experiment. The axial displacement of the gouge layer, i.e. its compaction or dilation, was measured using a DCDT (Direct Current Differential Transformer) with a resolution of c. 50 µm, which is installed on the stationary axis. The axial displacement as well as the torque, normal load, rotation velocity and displacement were measured with a sampling rate of 25 kHz.

2.2. Experimental Set-Up of the "Pressurized high-velocity" ("Phv") Apparatus

A total of 24 high-velocity, rotary-shear experiments were performed with the Phv apparatus under room-dry and controlled pore pressure conditions (Table 2). Experiments with the Phv apparatus were also performed at a target maximum slip velocity of c. 1 m/s but with a slower acceleration of 0.5 m/s^2. Additionally, in some experiments the gouge samples were pre-sheared for a displacement of c. 30 cm at a velocity of 1 mm/s (Table 2). The gouge holder used with the Phv apparatus has inner/outer diameters of 30 and 60 mm.

Pore fluid in the Phv apparatus is introduced to the gouge layer (marked yellow in Fig. 1b) through the stationary part of the gouge holder (grey parts in Fig. 1b). The fluid outlet is located in the center of the annular holder; thus, the pore fluid has to pass through the gouge material before passing into the fluid-outlet tube in the rotary part of the gouge holder (white parts in Fig. 1b) and further into the outlet tube within the stationary part. The saturated gouge is confined with inner and outer Teflon sleeves and several o-rings (Fig. 1b). Fluid pressure is monitored upstream and downstream of the sample using two pressure gauges and is adjusted via a servo-controlled moving piston. As the pressure gauges are located outside the sample chamber, the pore pressure cannot be perfectly controlled. Applied effective normal stresses and pore-fluid pressures ranged from 3 to 12 MPa and from 0.2 to 10.5 MPa, respectively (Table 2). The experiments were performed with room-dry and water-saturated calcite gouges, but without the use of strain-markers. The experimental data were recorded at a sampling rate of 1 kHz.

2.3. Sample Preparation and Analysis Techniques

The calcite gouge was derived by crushing pieces of Carrara marble. The dolomite gouge used for the strain markers in the SHIVA experiments was derived by crushing cohesive dolostones from the Foiana Tectonic Line (Fondriest et al., 2013). Both gouges were sieved to particle sizes <250 µm. For the experiments performed with SHIVA, 5 g of calcite gouge were distributed inside the gouge holder yielding a gouge layer thickness of c. 3 mm. Afterwards a c. 2 mm wide, subvertical (approx. $\pm 20^\circ$) dolomite strain marker was constructed perpendicular to both the imposed shear direction and the gouge layer boundaries (Fig. 2a). For SHIVA experiments with water-dampened gouges, 1 ml of distilled H_2O was added evenly to the top surface of the gouge layer using a pipette. The gouge was then pre-compacted using a pneumatic press yielding an initial gouge layer thickness of ca. 2.5 mm (Fig. 2a). For Phv experiments, 15 g of calcite gouge were used to obtain a gouge layer thickness of c. 3 mm. The gouge layer was pre-saturated by adding distilled water using a pipette. Full saturation was achieved using the pore-pressure system as described above.

After each experiment performed with SHIVA, a sample of the gouge layer containing the sheared strain marker was preserved in resin and cut (using a water-cooled saw) subparallel to the shear direction to obtain a cross-section through the sheared strain marker (Fig. 2b, c). Due to the annular sample geometry, maximum slip velocity and total displacement vary inside the gouge layer depending on the radial position. In the following, we thus report the “equivalent” velocity and displacement following Hirose and Shimamoto (2005). When preparing the sample, care was taken to cut the different samples at approximately the same radial positions to produce comparable results in terms of microstructural analysis and strain measurements.

Polished samples were coated with carbon or chrome for microstructural analysis using a JEOL JSM-6500F Field-Emission Scanning Electron Microscope (SEM) at the Istituto Nazionale di Geofisica e Vulcanologia (INGV) in Rome, Italy, a CamScan MX3000 SEM at the University of Padua and a LEO (Zeiss) 1530 Gemini High resolution thermally-aided Field Emission SEM at the Institute of Geology, Mineralogy and Geophysics of the Ruhr-Universität Bochum, Germany. Images were obtained in backscattered electron mode using an acceleration voltage of 8–20 kV and a working distance of 7.3–20 mm. In backscattered mode, the dolomite marker is easily distinguished from the surrounding calcite due to its darker grey color (Fig. 2a). The marker is sheared in the direction of slip and the finite strain γ at different positions within the gouge layer can be calculated from the angle of distortion φ using the relation $\gamma = \tan\varphi = dx/x$, where *x* is the thickness of the layer and *dx* the amount of horizontal displacement (Fig. 2d, e).

3. Results

3.1. Mechanical behavior of room-dry and water-dampened calcite gouges

In SHIVA experiments, the evolution of shear stress τ with displacement is highly reproducible for experiments conducted under the same conditions (i.e., the same normal stress and ambient conditions; Fig. 3a). At maximum slip velocities of 1 m/s the peak stress, τ_{peak}, ranges from c. 2.5 to c. 16 MPa at normal stresses σ_n ranging from 3 to 20 MPa (Table 3). This corresponds to an apparent peak friction coefficient $\mu = \tau/\sigma_n$ of c. 0.6–0.7, with higher values of the friction coefficient reached at higher normal stresses. The coefficient of friction is an “apparent” one because the pore pressure and thus the effective normal stress is not known in our water-dampened experiments. Following τ_{peak}, the gouges weaken to a steady-state shear stress τ_{ss} (Fig. 3a, Table 3).

The evolution of shear stress in the experiments performed with the Phv apparatus shows very similar behavior compared to the SHIVA experiments (Fig. 3b), although at a given normal stress the absolute shear stress values are slightly higher than in experiments conducted with SHIVA. The similar behavior of pure calcite gouge (i.e. Phv experiments in Fig. 3b) and calcite gouge containing a dolomite strain marker (i.e. SHIVA experiments in Fig. 3a) indicates that the dolomite marker has a negligible effect on the mechanical behavior.

Compaction of the gouge layer during the experiments also varies with ambient conditions. At the initiation of sliding, the water-dampened gouges compact slightly faster than the room-dry gouges (Fig. 3c), but after a displacement of about 0.1–0.2 m, the rate of compaction is higher in the room-dry than in the water-dampened experiments, yielding a similar net compaction in both room-dry and water-dampened experiments (c. 150–200 µm after a displacement of 0.5 m; corresponding to c. 5% of the starting layer thickness). The change in the rate of compaction in the room-dry samples broadly coincides with the onset of dynamic weakening in some experiments (Fig. 3d). No significant amount of transient dilation is observed in either room-dry or water-dampened gouges.

Peak stress in the experiments is reached after a strengthening phase (i.e. the slip distance prior to the onset of dynamic weakening) that is annotated schematically in Figures 3a and 3d. The length of the strengthening phase and its dependence on the applied normal stress is shown in Fig. 4a for both room-dry and wet experiments conducted using the SHIVA and Phv apparatus. The length of the strengthening phase generally decreases with increasing normal stress, but at normal stresses <12 MPa the length of the strengthening phase is up to two orders of magnitude longer in room-dry gouge experiments compared to wet gouges (Fig. 4a). Data from the SHIVA and Phv apparatus are comparable, lending confidence that our results are reproducible.

Although the acceleration was higher in experiments performed with SHIVA (6 m/s^2 compared to 0.5 m/s^2) the length of the strengthening phase under wet conditions is slightly longer than in Phv experiments (compare data at 8.5 MPa in Fig. 4a). Since dynamic weakening is predicted to occur faster at higher accelerations, i.e. when a certain critical velocity for weakening is reached, this result suggests that the effect of the different accelerations on the mechanical data is negligible compared to the influence of the pore fluid pressure. This is consistent with results by Niemeijer et al. (2011) who did not find a systematic dependence of the shear stress on the acceleration (see their Figure 7a).

For effective normal stresses of 3–21 MPa, the length of the strengthening phase decreases from c. 80 cm to c. 4 cm in the room-dry gouges, consistent with data in Smith et al. (2015) (Fig. 4a). In water-dampened (SHIVA) and water-saturated (*Phv*) gouges, the length of the strengthening phase decreases from c. 15 mm to c. 0.5 mm at effective normal stresses of 1–12 MPa. At normal stresses exceeding 12 MPa, two water-dampened experiments performed with SHIVA suggest that the length of the strengthening phase may increase to values similar to those in room-dry conditions (Fig. 4a). However, in these two experiments performed at relatively high normal stresses, water and gouge were observed to escape from the gouge holder after a few centimeters of slip, and thus more experiments are required to test if this effect is real or due to gouge loss. There is no significant effect of the pre-shearing at low-velocity performed with the Phv apparatus on the length of the strengthening phase.

After the strengthening phase, dynamic weakening initiates and the gouge weakens to a steady-state shear stress (Fig. 3). As shown in Fig. 4b, the degree of weakening increases with normal stress. In the experiments performed with SHIVA, for a given normal stress within the tested range there is no significant dependence of the amount of weakening on the ambient conditions. However, in the experiments performed with the Phv apparatus, the amount of weakening appears to be higher under room-dry conditions.

3.2. Progressive microstructure development

The microstructure of the sheared calcite gouges evolves with increasing displacement, as previously described in dry calcite gouges by Bullock et al. (2015) and Smith et al. (2015) and in gouges of different lithologies (e.g., Oohashi et al., 2013). We were not able to preserve a room-dry sample with a displacement of 0.01 m containing a strain marker due to its fragility after such short displacements. However, Smith et al. (2015) observed that after a displacement of 0.01 m (prior to the onset of dynamic weakening), room-dry calcite gouges contain a well-defined, up to 20 µm thick shear band that developed close to the gouge layer boundary (Fig. 5a). The grains within the shear band were smaller in size and more compacted than the surrounding material. Under the same conditions as applied by Smith et al. (2015) in room-dry experiments (i.e., a total displacement of 0.01 m, normal stress of 8.5 MPa, and a target velocity of 1 m/s), no such fine-grained, compacted shear bands were observed in water-dampened samples (s959, Table 1) (Fig. 5b). Instead, the particles are angular to sub-angular in shape and the porosity is high. Although no high-strain shear band can be observed, the dolomite marker is inclined in the direction of shearing due to an incipient boundary shear. The dolomite material seems to have a slightly smaller grain size, indicating that comminution was at least starting to localize close to the upper surface of the gouge layer.

At larger total displacements of 0.13–0.2 m, the zone of comminution has expanded into the gouge layer in both room-dry and water-dampened gouges (Fig. 5c, d). Larger particles, which are still relatively angular and range from several tens of µm up to c. 150 µm in size, are embedded in a fine-grained matrix with particle sizes on the order of a few tens of µm or less. The dolomite marker is sheared towards parallelism with the gouge layer boundaries. In the layer closest to the upper surface of the gouge layer, dolomite grains are mixed with the fine-grained calcite that makes up this zone. Additionally, several R-type shear bands (terminology after Logan et al., 1979) developed in the room-dry sample, inclined at c. 20° to gouge layer boundaries, accommodating some strain as is evidenced by an offset of the dolomite marker (Fig. 5c).

After a total displacement of 0.43 m, a discrete slip surface developed in both room-dry and water-dampened gouges (Fig. 5e, f). The slip surface cuts through a zone of highly-comminuted and -compacted gouge c. 125–600 µm thick. In this high-strain layer many larger particles, generally several 10s of µm in size, are mixed in a matrix with a particle size of a few µms. Several secondary shear bands, generally oriented sub-parallel to the gouge layer boundary (Y-shears), may be found within the high-strain zone. The transition of the high-strain to the lower-strain zone, marked by the change in particle size and porosity, is rather abrupt in both room-dry and water-dampened samples (Fig. 5e). After a total displacement of 0.43 m in our water-dampened conditions (Fig. 5f), calcite grains adjacent to the principal slip surface, in a zone 10–40 µm thick, have a relatively angular shape, with grain sizes in the order of 500 nm. They generally show a shape-preferred orientation with the long axis sub-parallel to the principal slip surface consistent with the imposed sense of shear, resembling mylonitic shear zones (e.g., Herwegh and Handy, 1998; Snoke et al., 1998). This appearance suggests recrystallization (Smith et al., 2013) and is consistent with the observations in room-dry gouge samples with a total displacement of 0.35 m by Smith et al. (2015).

At displacements exceeding 1 m, the size and shape of the particles and the distortion of the marker in the lower-strain zones of the gouge layer does not appear to have further evolved (Fig. 5g, h). Particles in the bulk gouge are still relatively angular and up to 200 µm in size. In the high-strain layer, however, zones of recrystallization – where present – seem to have expanded or secondary, boundary-parallel shear zones are more established (Fig. 5g, h).

In summary, no significant differences in the microstructure of room-dry and water-dampened gouges could be observed in the preserved samples. In both cases, the high-strain zone evolves from a broad zone of comminuted material that is only slightly compacted and contains several poorly-developed shear bands, to a zone of highly-comminuted and compacted gouge cut by a discrete principal slip surface.

3.3. Quantitative strain analysis

From the 18 strain-marker experiments performed with SHIVA, 14 preserved a relatively intact strain marker that could be used to quantify the strain distribution in the gouge layer after a range of total displacements. The estimated errors in our strain measurements (Fig. 6) are relatively large for a number of reasons. Firstly, the strain was not always evenly distributed within the same textural zone in the gouge; secondly, the margins of the marker (i.e. the left and the right marker boundaries in Fig. 5) were sheared to a different degree in most samples, requiring that the strain be estimated from the average angle of distortion; thirdly, the shape of the strain marker as initially prepared in the gouge layers was not identical in all samples, although the thickness of the marker was approximately the same. Finally, the samples were highly fractured in many cases (especially in the high-normal stress experiments) and thus the margins of the strain markers are disrupted. Despite the difficulties encountered, most of the strain markers were sufficiently well preserved that they could be used to evaluate the strain distribution across the bulk of the gouge layers.

Within the lower-strain zones, the boundaries of the marker are sheared slightly in the direction of slip, but are still relatively straight and can easily be traced (annotated in Fig. 2e). The angle of distortion (i.e., the angle between the original and the sheared marker, Fig. 2c) ranges from c. 0°–60°, resulting in relatively low strains of 0–2 (Fig. 6a). Further towards the principal slip surface, the marker is sheared towards parallelism with the gouge layer boundaries (Fig. 5g, annotated in Fig. 2e). There is a gradual transition in texture from the low- to the intermediate-strain zone and no sharp change in the distortion angle of the marker boundary. In the intermediate-strain zone, the dolomite marker still forms a largely intact layer but towards the principal slip surface it begins to disaggregate (e.g., Fig. 5d) and single dolomite particles can be found dispersed in the calcite matrix. In the high-strain zone (Fig. 5g), the marker cannot be traced as an intact layer and only single dolomite grains are found embedded in the highly-comminuted matrix. The finite strain in this zone can thus be calculated from the finite strain measured in the low- and intermediate-strain zones subtracted from the bulk strain (the ratio of the total displacement and the thickness of the initial gouge layer that was determined from the post-experimental thickness of the gouge layer and the amount of compaction).

The quantitative strain data obtained separately for these three textural zones are shown in Fig. 6. For experiments performed under a normal stress of 8.5 MPa, the finite strain in the low- and intermediate strain zones does not show a significant dependence on the total displacement (Fig. 6a, b). Additionally, the finite strain is similar in room-dry and water-dampened samples. The strain hosted in the high-strain zone correlates with the total displacement (Fig. 6c), increasing approximately linearly with increasing total displacement. This indicates that after short displacements, almost all strain is accommodated in the high-strain zone. At short total displacements (≤0.43 m), the strain hosted in the high-strain zone is larger in the water-dampened experiments than in the room-dry experiments (Fig. 6c). The quantitative strain data for the low-, intermediate-, and high-strain zones (Fig. 6a, b, and c, respectively) show no dependence on the applied normal stress.

4. Discussion

The main aim of this study was to investigate the effect of water on the strain localization process in calcite gouges. In the following, we first discuss how strain localization progresses with increasing displacement. No significant microstructural differences were observed in room-dry and water-saturated samples, even though the mechanical behavior of the calcite gouge is strongly influenced by the presence of water. Secondly, we review potential dynamic weakening mechanisms that could lead to the observed differences in mechanical behavior. Finally, we discuss the implications of our experimental results for earthquakes occurring in natural carbonate-bearing fault zones.

4.1. Progressive strain localization

Scanning electron microscope analysis of our room-dry and water-dampened samples sheared to comparable total displacements revealed no significant microstructural differences (Fig. 5, 7). In both room-dry and water-dampened samples, the marker was slightly sheared after a total displacement of c. 1 cm (Fig. 5a, b). At displacements larger than c. 0.2 m, a discrete principal slip surface developed, indicating a high degree of localization in both dry and wet gouges (Fig. 5e-h). The microstructures suggest that strain localization progresses at a similar rate in room-dry and water-dampened gouges.

Likewise, the quantitative strain data obtained from the distortion of the strain markers do not show a significant difference in the amount of strain hosted in the low-, intermediate-, or high-strain zones of the room-dry and water-dampened samples. No clear dependence on the total displacement is evident in the lower-strain regions. The strain hosted in the high-strain zone, however, increases approximately linearly with total displacement (Fig. 6c) indicating that after localization is achieved most slip is hosted in this principal slip zone independent of the ambient conditions. Thus, a substantial strain and velocity gradient is present between the high- and the low-strain zones. This conclusion is supported by the presence of recrystallized calcite grains (Fig. 5f) within a ≤40 µm wide zone adjacent to the principal slip surface of water-dampened samples, consistent with observations in dry calcite gouge (Smith et al., 2015), indicating a higher degree of frictional heating close to the principal slip surface. Although most slip is hosted in the principal slip zone once localization is achieved, microstructural observations of Smith et al. (2015) showed that the grain size in the bulk of the gouge layer continues to decrease, suggesting at least some distributed deformation. Part of the strain in the bulk of the gouge layer is likely also accommodated on Y-, R1- and P-shears that are observed in many of our gouge samples.

The conclusion that the strain localization process is similar in room-dry and water-dampened gouges seems to contrast with the mechanical data showing a pronounced difference between experiments conducted in dry and wet conditions (Fig. 3, 4, 7). In our high-velocity calcite gouge experiments, dynamic weakening occurs much more abruptly in the presence of water (Fig. 3, 4a). The amount of water in the gouge layer appears to have a minor effect on the mechanical behavior, as gouges prepared with only 20 wt% water (SHIVA experiments) behaved in a similar manner to the completely saturated gouges deformed with controlled pore pressure (Phv experiments).

In previous studies, the initial strengthening phase observed in the mechanical data has been attributed to progressive localization of strain to a high-strain shear band that has to evolve to a critical state prior to weakening (e.g., by Marone et al., 1992; Beeler et al., 1996; Rathbun and Marone, 2010; Smith et al., 2015). Because the strengthening phase was often accompanied by layer dilation, thought to be due to shear dilatancy during rolling and comminution of particles (e.g., Mandl et al., 1977), it was concluded that the strengthening phase is associated with some distributed deformation rather than fully localized shear (Marone et al., 1990; Rathbun and Marone, 2010). In our experiments, no transient dilation was observed during or after the strengthening phase, possibly due to a different initial state of gouge compaction. The observed larger rate of compaction in the water-dampened gouges compared to the room-dry material prior to weakening (Fig. 3c) could be caused by some loss of water from the sample chamber. It might also suggest that the strain is in fact localizing faster in water-dampened than in room-dry conditions, albeit to a small degree that is not shown in the microstructures. In this case, the change in the compaction rate with the onset of dynamic weakening in room-dry conditions (Fig. 3d) might likewise suggest a switch from rather distributed to more localized shear.

Based on their mechanical and microstructural data, Smith et al. (2015) concluded that localization of slip to a high-strain shear band is a necessary precursor to dynamic weakening in dry calcite gouges. In water-dampened gouges, however, as argued above, there is no microstructural evidence of strain localization to a high-strain shear band prior to (almost instantaneous) dynamic weakening (Fig. 5b, 7). Additionally, high-velocity friction experiments on solid Carrara marble cylinders (Violay et al., 2013), where slip is effectively localized from the beginning of the experiment, also showed a much faster weakening in saturated conditions, thus supporting the conclusion that it is not faster localization causing the faster weakening in water-dampened conditions. It follows that dynamic weakening in water-dampened gouges likely occurs *prior* to complete strain localization. Potential mechanisms that would lead to faster dynamic weakening in water-dampened conditions are discussed below (Section 4.2).

The close agreement of the shear stress evolution in room-dry and water-dampened conditions during the first ~8 mm of slip (Figs. 3d) gives rise to the idea that what we measure as strengthening in water-dampened conditions might in fact be an apparent strengthening induced by the stiffness of the apparatus. The stiffness of the columns of the apparatus should increase with increasing normal load, thus leading to the observed decrease in the apparent strengthening phase with increasing normal stress (Fig. 4a). The long strengthening phase in water-dampened conditions at normal stresses of 15 and 20 MPa may be due to loss of water during sample loading and compaction, or, quite to the contrary, due to a thermal or mechanical pressurization of the pore fluids, effectively decreasing the normal stress. In the room-dry conditions, the dependence on the normal stress is possibly due to higher temperatures achieved in the slipping zone at higher normal stresses accelerating the onset of thermal weakening mechanisms. The decrease in the length of the strengthening phase with increasing normal stress is consistent with the results obtained by Smith et al. (2015) in room-dry conditions and thus with their conclusion that triggering of dynamic weakening in calcite-bearing fault zones is dependent on the normal stress, and large coseismic slip may be impeded at shallow crustal depths due to a particularly long strengthening phase (in addition to the stabilizing effect of gouges present in a fault zone during the earthquake nucleation phase; Marone and Scholz, 1988).

4.2. Potential dynamic weakening mechanisms

The observed rapid dynamic weakening in water-dampened conditions suggests that the active weakening mechanisms are either more efficient or different from those acting in relatively dry conditions. In the following, we discuss possible weakening mechanisms such as the formation of a fluid layer, thermal pressurization, flash weakening, and the activation of grain-size dependent mechanisms and evaluate their potential to accelerate weakening in the presence of fluids.

A simple explanation for the rapid weakening could be the formation of a lubricating water layer along one side of the gouge layer and/or the principal slip surface. However, this does not explain the slightly higher steady state shear stress observed in water-dampened conditions (Fig. 3a, b). Similarly, thermal pressurization of the pore fluid is not likely to accelerate weakening. Because water can escape from the holder, no excess pore pressure can be maintained in the experiments with SHIVA. Expulsion of water from the gouge layer will occur readily in the first few centimeters of slip (i.e., when the dynamic weakening occurs), because no impermeable principal slip surface has yet developed. The similarity of the mechanical data from SHIVA and Phv experiments (Fig. 3a, b) suggests that in the experiments with the Phv apparatus pore pressure is not elevated or has a negligible effect on the mechanical behavior. This conclusion is consistent with results by Violay et al. (2015), who found that thermal pressurization of pore fluids does not play an important role in the dynamic weakening of cohesive carbonate rocks.

Flash weakening might play a role in both room-dry and water-dampened gouges sheared at high velocity. As modeled by Violay et al. (2014), the temperature rise due to frictional heating in water-dampened and water-saturated calcite gouge or solid rocks is not significantly lower than in room-dry or vacuum conditions. However, flash weakening would require a high degree of strain localization, which was not observed in the water-dampened gouges prior to the onset of dynamic weakening. It was suggested by Violay et al. (2014) that weakening in their water-dampened solid carbonate cylinders was accelerated by subcritical crack growth due to stress corrosion (Atkinson and Meredith, 1987). Stress corrosion is much more efficient in fluid-saturated conditions because the fracture surface energy of calcite is 2–3 times lower in the presence of water resulting in faster crack propagation (Røyne et al., 2011). Possibly, enhanced stress corrosion due to pore fluids could accelerate cataclasis in our water-dampened gouges (taking effect already during the set-up of the experiment) thus leading to the formation of nanograins (De Paola et al., 2015) occurring faster for water-dampened than for room-dry conditions. The formation of nanograins might then cause a transition from brittle deformation to grain-size sensitive grain boundary-sliding mechanisms causing, in turn, the decrease in the shear stress observed during dynamic weakening (De Paola et al., 2015; Green et al., 2015). Whether enhanced cataclasis due to subcritical crack growth is efficient enough to induce rapid grain-size dependent weakening mechanism remains to be resolved.

Instead of enhanced cataclasis, phase transformation was proposed as an alternative mechanism to form nanograins (Green et al., 2015). In the case of dolomite, decarbonation led to the formation of oxide grains with sizes less than c. 50 nm. This process of forming nanograins by phase transformation is likely relevant to calcite gouges as dolomite and calcite are chemically similar. In fact, in the presence of water, the decarbonation temperature for calcite is lower than in dry conditions, possibly explaining the faster dynamic weakening in the water-dampened gouges.

It was found that the steady-state shear stress was lower and the amount of weakening was higher under room-dry relative to water-dampened conditions (Fig. 3a, b, Fig. 4b). Possibly, the steady-state stress and the amount of weakening is also controlled by crystal-plastic deformation processes such as grain boundary sliding aided by diffusion creep. Due to the grain-size dependence of diffusion creep in carbonate rocks (Schmid et al., 1977), a slightly smaller grain size in room-dry conditions might be responsible for the lower steady-state shear stress (assuming similar diffusion rates). Microstructural evidence for crystal-plastic deformation processes is provided by recrystallized grains lining the principal slip surface (Fig. 5f). However, to identify whether nanograins are present on the slip surfaces of our samples and if the grain size is different in the room-dry and water-dampened sheared gouges, higher-resolution microstructural work needs to be carried out.

4.3. Implications for natural faults

In nature, frictional sliding on a pre-existing fault will initiate if a critical shear stress due to tectonic loading is reached, potentially leading to dynamic weakening of the fault, i.e., an earthquake instability. Velocity-strengthening behavior of the fault rocks might lead to an arrest of rupture prior to catastrophic failure. In our rotary-shear gouge experiments, simulating frictional sliding on a pre-existing fault, such a potentially stabilizing strengthening phase is observed under room-dry conditions. In the water-dampened and saturated experiments the strengthening phase was significantly shorter, implying that at shallow depths, gouge-bearing faults in carbonates will be more prone to rapid dynamic weakening in the presence of water. Violay et al. (2013) reached a similar conclusion for solid (cohesive) samples of carbonate. Faster weakening in wet conditions occurs if only a relatively small amount of water (only 20 wt% H_2O were used in our water-dampened experiments with SHIVA, Fig. 3a) is present and also if the fault contains pressurized fluids. This has important implications for the coseismic rupture behavior of faults. As suggested by our experimental results (Fig. 3, 4a), dynamic weakening will occur faster if water is present in the slip zones. Local evidence of the involvement of water during faulting was indeed found by several studies of carbonate-bearing faults (De Paola et al., 2008; Collettini et al., 2009; Smith et al., 2011). Additionally, an heterogeneous distribution of fluids in a fault zone might explain some of the slip distribution complexity observed during earthquake sequences in carbonate (Cirella et al., 2009; Pino and Di Luccio, 2009; Di Stefano et al., 2011). For instance, the heterogeneous coseismic slip distribution of the 2009 M_w6.3 L'Aquila mainshock correlates well with the near-fault pattern of aftershocks that cluster around the high-slip patches (Cirella et al., 2009) and that were attributed to the presence of high-pressure fluids at depth (Chiodini et al., 2011; Miller, 2013).

5. Conclusion

A series of intermediate- to high-velocity rotary-shear experiments was conducted on synthetic calcite gouges prepared with dolomite strain markers. The strain marker experiments were conducted with varying total displacements (0.011–2.5 m), normal stresses (3–21 MPa) and ambient conditions (room-dry and water-dampened) to study strain-localization processes and to test the dependence of the strain distribution on these different experimental variables.

The mechanical behavior of room-dry and water-dampened gouges sheared at 1 m/s is significantly different: while the room-dry gouges show a prolonged strengthening phase prior to dynamic weakening, the water-dampened gouges dynamically weaken nearly instantaneously to a steady-state shear stress that is slightly higher than in room-dry conditions. Microstructural analysis of the sheared dolomite markers revealed progressive strain localization to a thin (125–600 μm) high-strain layer that developed after several cm of slip in both room-dry and water-saturated conditions. The strain hosted in the bulk of the gouge layer did not change significantly with increasing total displacement suggesting that, once formed, the high-strain slipping zone and slip surface accommodated most of the subsequent displacement and that a substantial strain and velocity gradient exists in the thin layer of gouge. No significant differences in the degree or timing of strain localization were observed in room-dry and water-dampened gouges, leading to the conclusion that faster dynamic weakening in water-dampened conditions is not because of faster localization but due to a different or more efficient weakening mechanism than in room-dry conditions. The faster dynamic weakening in the presence of fluids might explain some of the observed slip distribution complexity in natural carbonate-bearing fault zones.

6. Acknowledgements

Andrea Cavallo, Rolf Neuser and Leonardo Tauro are thanked for assistance with SEM analysis. Elena Spagnuolo, Fabio Ferri and Kentaro Hatakeda are thanked for technical assistance. This work was supported by Ca.Ri.Pa.Ro.; a 2014 University of Otago Research Grant; the Marsden Fund Council (project UOO1417), administered by the Royal Society of New Zealand; the European Research Council Starting Grant USEMS [grant no. 205175], the European Research Council Consolidator Grant NOFEAR [grant no. 614705] and the JSPS KAKENHI [grant no. 16H04064]. Anne Pluymakers and an anonymous reviewer are thanked for valuable suggestions that helped to improve this manuscript.

7. References

Aben, F., M. L. Doan, et al. (2016). "Dynamic fracturing by successive coseismic loadings leads to pulverization in active fault zones." Journal of Geophysical Research: Solid Earth **121**(4): 2338-2360.

Atkinson, B. K. and P. G. Meredith (1987). "The theory of subcritical crack growth with applications to minerals and rocks." Fracture mechanics of rock **2**: 111-166.

Beeler, N., T. Tullis, et al. (1996). "Frictional behavior of large displacement experimental faults." Journal of Geophysical Research: Solid Earth (1978–2012) **101**(B4): 8697-8715.

Ben-Zion, Y. and C. G. Sammis (2003). "Characterization of fault zones." Pure and Applied Geophysics **160**(3-4): 677-715.

Boullier, A. M., E. C. Yeh, et al. (2009). "Microscale anatomy of the 1999 Chi-Chi earthquake fault zone." Geochemistry Geophysics Geosystems **10**.

Bullock, R. J., N. De Paola, et al. (2015). "An experimental investigation into the role of phyllosilicate content on earthquake propagation during seismic slip in carbonate faults." Journal of Geophysical Research: Solid Earth **120**(5): 3187-3207.

Chester, F. M. and J. S. Chester (1998). "Ultracataclasite structure and friction processes of the Punchbowl fault, San Andreas system, California." Tectonophysics **295**(1): 199-221.

Chester, F. M., J. P. Evans, et al. (1993). "INTERNAL STRUCTURE AND WEAKENING MECHANISMS OF THE SAN-ANDREAS FAULT." Journal of Geophysical Research-Solid Earth **98**(B1): 771-786.

Chiodini, G., S. Caliro, et al. (2011). "Geochemical evidence for and characterization of CO 2 rich gas sources in the epicentral area of the Abruzzo 2009 earthquakes." Earth and Planetary Science Letters **304**(3): 389-398.

Cirella, A., A. Piatanesi, et al. (2009). "Rupture history of the 2009 L'Aquila (Italy) earthquake from non‐linear joint inversion of strong motion and GPS data." Geophysical Research Letters **36**(19).

Collettini, C., N. De Paola, et al. (2009). "Insights on the geometry and mechanics of the Umbria–Marche earthquakes (Central Italy) from the integration of field and laboratory data." Tectonophysics **476**(1): 99-109.

De Paola, N., F. Agosta, et al. (2012). Constraints on fault dynamic weakening mechanisms from natural slip surfaces in carbonate faults. AGU Fall Meeting Abstracts.

De Paola, N., C. Collettini, et al. (2008). "Fault zone architecture and deformation processes within evaporitic rocks in the upper crust." Tectonics **27**(4).

De Paola, N., T. Hirose, et al. (2011). "Fault lubrication and earthquake propagation in thermally unstable rocks." Geology **39**(1): 35-38.

De Paola, N., R. E. Holdsworth, et al. (2015). "Can grain size sensitive flow lubricate faults during the initial stages of earthquake propagation?" Earth and Planetary Science Letters **431**: 48-58.

Di Stefano, R., C. Chiarabba, et al. (2011). "Fault zone properties affecting the rupture evolution of the 2009 (Mw 6.1) L'Aquila earthquake (central Italy): Insights from seismic tomography." Geophysical Research Letters **38**(10).

Di Toro, G., A. Niemeijer, et al. (2010). "From field geology to earthquake simulation: a new state-of-the-art tool to investigate rock friction during the seismic cycle (SHIVA)." RENDICONTI LINCEI **21**(1): 95-114.

Faulkner, D., T. Mitchell, et al. (2011). "Stuck in the mud? Earthquake nucleation and propagation through accretionary forearcs." Geophysical Research Letters **38**(18).

Fondriest, M., S. A. Smith, et al. (2012). "Fault zone structure and seismic slip localization in dolostones, an example from the Southern Alps, Italy." Journal of structural Geology **45**: 52-67.

Fondriest, M., S. A. F. Smith, et al. (2013). "Mirror-like faults and power dissipation during earthquakes." Geology **41**(11): 1175-1178.

Goldsby, D. L. and T. E. Tullis (2011). "Flash heating leads to low frictional strength of crustal rocks at earthquake slip rates." Science **334**(6053): 216-218.

Green, H., F. Shi, et al. (2015). "Phase transformation and nanometric flow cause extreme weakening during fault slip." Nature Geoscience **8**(6): 484-489.

Han, R. and T. Hirose (2012). "Clay-clast aggregates in fault gouge: An unequivocal indicator of seismic faulting at shallow depths?" Journal of Structural Geology **43**: 92-99.

Han, R., T. Hirose, et al. (2010). "Strong velocity weakening and powder lubrication of simulated carbonate faults at seismic slip rates." Journal of Geophysical Research: Solid Earth **115**(B3).

Han, R., T. Shimamoto, et al. (2007). "Ultralow friction of carbonate faults caused by thermal decomposition." Science **316**(5826): 878-881.

Heermance, R., Z. K. Shipton, et al. (2003). "Fault structure control on fault slip and ground motion during the 1999 rupture of the Chelungpu fault, Taiwan." Bulletin of the seismological society of America **93**(3): 1034-1050.

Herwegh, M. and M. Handy (1998). "The origin of shape preferred orientations in mylonite: inferences from in-situ experiments on polycrystalline norcamphor." Journal of Structural Geology **20**(6): 681-694.

Hirose, T. and T. Shimamoto (2005). "Growth of molten zone as a mechanism of slip weakening of simulated faults in gabbro during frictional melting." Journal of Geophysical Research-Solid Earth **110**(B5).

Kitajima, H., J. S. Chester, et al. (2010). "High-speed friction of disaggregated ultracataclasite in rotary shear: Characterization of frictional heating, mechanical behavior, and microstructure evolution." Journal of Geophysical Research-Solid Earth **115**.

Kohli, A. H., D. L. Goldsby, et al. (2011). "Flash weakening of serpentinite at near ‐ seismic slip rates." Journal of Geophysical Research: Solid Earth **116**(B3).

Lachenbruch, A. H. (1980). "Frictional heating, fluid pressure, and the resistance to fault motion." Journal of Geophysical Research: Solid Earth **85**(B11): 6097-6112.

Logan, J., M. Friedman, et al. (1979). "Experimental studies of simulated gouge and their application to studies of natural fault zones." US Geol. Surv. Open File Rep **1978**: 305-343.

Mandl, G., L. De Jong, et al. (1977). "Shear zones in granular material." Rock Mechanics **9**(2-3): 95-144.

Marone, C., B. Hobbs, et al. (1992). "Coulomb constitutive laws for friction: Contrasts in frictional behavior for distributed and localized shear." Pure and Applied Geophysics **139**(2): 195-214.

Marone, C., C. B. Raleigh, et al. (1990). "Frictional behavior and constitutive modeling of simulated fault gouge." Journal of Geophysical Research: Solid Earth **95**(B5): 7007-7025.

Marone, C. and C. Scholz (1988). "The depth of seismic faulting and the upper transition from stable to unstable slip regimes." Geophysical Research Letters **15**(6): 621-624.

Miller, S. A. (2013). "The role of fluids in tectonic and earthquake processes." Advances in Geophysics **54**: 1-46.

Morrow, C., D. E. Moore, et al. (2000). "The effect of mineral bond strength and adsorbed water on fault gouge frictional strength." Geophysical research letters **27**(6): 815-818.

Niemeijer, A., G. Di Toro, et al. (2011). "Frictional melting of gabbro under extreme experimental conditions of normal stress, acceleration, and sliding velocity." Journal of Geophysical Research: Solid Earth **116**(B7).

Oohashi, K., T. Hirose, et al. (2013). "Graphite as a lubricating agent in fault zones: An insight from low‐to high‐velocity friction experiments on a mixed graphite‐quartz gouge." Journal of Geophysical Research: Solid Earth **118**(5): 2067-2084.

Pavlis, T. L., L. F. Serpa, et al. (1993). "Role of seismogenic processes in fault-rock development: An example from Death Valley, California." Geology **21**(3): 267-270.

Pino, N. A. and F. Di Luccio (2009). "Source complexity of the 6 April 2009 L'Aquila (central Italy) earthquake and its strongest aftershock revealed by elementary seismological analysis." Geophysical Research Letters **36**(23).

Platt, J. D., J. W. Rudnicki, et al. (2014). "Stability and localization of rapid shear in fluid‐saturated fault gouge: 2. Localized zone width and strength evolution." Journal of Geophysical Research: Solid Earth.

Proctor, B., T. Mitchell, et al. (2014). "Dynamic weakening of serpentinite gouges and bare surfaces at seismic slip rates." Journal of Geophysical Research: Solid Earth **119**(11): 8107-8131.

Rathbun, A. P. and C. Marone (2010). "Effect of strain localization on frictional behavior of sheared granular materials." Journal of Geophysical Research: Solid Earth **115**(B1).

Rempel, A. W. and J. R. Rice (2006). "Thermal pressurization and onset of melting in fault zones." Journal of Geophysical Research: Solid Earth (1978–2012) **111**(B9).

Rockwell, T. K. and Y. Ben‐Zion (2007). "High localization of primary slip zones in large earthquakes from paleoseismic trenches: Observations and implications for earthquake physics." Journal of Geophysical Research: Solid Earth **112**(B10).

Rowe, C. D., Å. Fagereng, et al. (2012). "Signature of coseismic decarbonation in dolomitic fault rocks of the Naukluft Thrust, Namibia." Earth and Planetary Science Letters **333–334**: 200-210.

Røyne, A., J. Bisschop, et al. (2011). "Experimental investigation of surface energy and subcritical crack growth in calcite." Journal of Geophysical Research: Solid Earth **116**(B4).

Sawai, M., T. Shimamoto, et al. (2012). "Reduction in BET surface area of Nojima fault gouge with seismic slip and its implication for the fracture energy of earthquakes." Journal of Structural Geology **38**: 117-138.

Schmid, S., J. Boland, et al. (1977). "Superplastic flow in finegrained limestone." Tectonophysics **43**(3): 257-291.

Scruggs, V. and T. Tullis (1998). "Correlation between velocity dependence of friction and strain localization in large displacement experiments on feldspar, muscovite and biotite gouge." Tectonophysics **295**(1): 15-40.

Sibson, R. H. (1986). "Brecciation processes in fault zones: inferences from earthquake rupturing." Pure and Applied Geophysics **124**(1-2): 159-175.

Sibson, R. H. (2003). "Thickness of the seismic slip zone." Bulletin of the Seismological Society of America **93**(3): 1169-1178.

Siman-Tov, S., E. Aharonov, et al. (2013). "Nanograins form carbonate fault mirrors." Geology **41**(6): 703-706.

Smith, S., S. Nielsen, et al. (2015). "Strain localization and the onset of dynamic weakening in calcite fault gouge." Earth and Planetary Science Letters **413**: 25-36.

Smith, S. A. F., A. Billi, et al. (2011). "Principal Slip Zones in Limestone: Microstructural Characterization and Implications for the Seismic Cycle (Tre Monti Fault, Central Apennines, Italy)." Pure and Applied Geophysics **168**(12): 2365-2393.

Smith, S. A. F., G. Di Toro, et al. (2013). "Coseismic recrystallization during shallow earthquake slip." Geology **41**(1): 63-66.

Snoke, A. W., J. Tullis, et al. (1998). Fault-related rocks: A photographic atlas, Princeton University Press.

Tadai, O., W. Tanikawa, et al. (2009). Design of new frictional testing machine for shallow fault materials. AGU Fall Meeting Abstracts.

Tanikawa, W., H. Mukoyoshi, et al. (2012). "Experimental investigation of the influence of slip velocity and temperature on permeability during and after high-velocity fault slip." Journal of Structural Geology **38**: 90-101.

Togo, T. and T. Shimamoto (2012). "Energy partition for grain crushing in quartz gouge during subseismic to seismic fault motion: an experimental study." Journal of Structural Geology **38**: 139-155.

Ujiie, K. and A. Tsutsumi (2010). "High-velocity frictional properties of clay-rich fault gouge in a megasplay fault zone, Nankai subduction zone." Geophysical Research Letters **37**.

Verberne, B., C. Spiers, et al. (2014a). "Frictional properties and microstructure of calcite-rich fault gouges sheared at sub-seismic sliding velocities." Pure and Applied Geophysics **171**(10): 2617-2640.

Verberne, B. A., J. H. de Bresser, et al. (2013). "Nanocrystalline slip zones in calcite fault gouge show intense crystallographic preferred orientation: Crystal plasticity at sub-seismic slip rates at 18–150° C." Geology **41**(8): 863-866.

Verberne, B. A., C. He, et al. (2010). "Frictional properties of sedimentary rocks and natural fault gouge from the Longmen Shan fault zone, Sichuan, China." Bulletin of the Seismological Society of America **100**(5B): 2767-2790.

Verberne, B. A., O. Plümper, et al. (2014b). "Superplastic nanofibrous slip zones control seismogenic fault friction." Science **346**(6215): 1342-1344.

Violay, M., G. Di Toro, et al. (2015). "Thermo-mechanical pressurization of experimental faults in cohesive rocks during seismic slip." Earth and Planetary Science Letters **429**: 1-10.

Violay, M., S. Nielsen, et al. (2014). "Effect of water on the frictional behavior of cohesive rocks during earthquakes." Geology **42**(1): 27-30.

Violay, M., S. Nielsen, et al. (2013). "Pore fluid in experimental calcite-bearing faults: Abrupt weakening and geochemical signature of co-seismic processes." Earth and Planetary Science Letters **361**: 74-84.

Yao, L., T. Shimamoto, et al. (2013). "Rapid postseismic strength recovery of Pingxi fault gouge from the Longmenshan fault system: Experiments and implications for the mechanisms of high ‐ velocity weakening of faults." Journal of Geophysical Research: Solid Earth **118**(8): 4547-4563.

8. Figure Captions

Figure 1: Experimental Set-Up. a) Annular sample holder used with SHIVA. Grey parts (including the base discs) and white parts slide against each other. Springs ensure that the applied load is borne by the gouge material, highlighted in yellow. b) Annular steel-and Teflon sample holder used with the Phv apparatus. Grey parts are stationary, white parts are rotating. Light grey areas depict inner and outer Teflon sleeves, confining the gouge in its chamber which size is reduced using porous spacers. O-rings (black circles) seal pore fluid in the system. *In* and *Out* label fluid in- and outlet paths, respectively.

Figure 2: Starting Material and Sample Preparation. a) Photograph of the dolomite marker prior to shearing prepared within the calcite starting material and backscattered electron image of section through the starting gouge layer showing the unsheared dolomite strain marker (dark material) in the uncomminuted calcite matrix (lighter-colored material). b) Sketch of a piece of the sheared sample illustrating how the preserved sample was cut to obtain a cross-section through the strain-marker for microstructure analysis. c) Sketch showing the part of the sheared gouge layer which can typically be preserved (shown in grey) reaching from the principal slip surface (PSS; solid horizontal line) close to the upper base disc to the lower base disc. Curved lines depict roughness of the base discs. Dotted lines show approximate boundaries of the low, intermediate (“Int.”) and high-strain zones with respect to the sheared strain marker (red lines). d) Sketch of an idealized strained marker (after Scruggs and Tullis, 1998). The strain γ was calculated from the angle of distortion ϕ as illustrated. e) Backscattered electron image of a sheared marker marked with the red line (experiment s943), illustrating the difficulties in assigning the low-, intermediate-, and high-strain zones and in determining the angles of the marker for each zone. For the case shown here, it was decided to calculate the angles of the marker boundaries marked with the solid lines (blue for low-, black for intermediate-strain zone) based on the degree of comminution of the material, rather than those marked with the dotted lines, which could also have been plausible and which were thus included in the error of the strain value.

Figure 3: Mechanical Data. a) Shear stress vs. equivalent displacement for experiments conducted with SHIVA using a target slip rate of 1 m/s and an acceleration of 6 m/s^2. Color coding corresponds to different ambient conditions and normal stresses used (see legend, valid for all subplots). The strengthening phase, i.e. the slip distance to the onset of dynamic weakening, is indicated with double-headed arrows. A slight misalignment of the axial columns of the apparatus causes oscillations in the shear stress, which are more severe at higher normal stresses. b) Shear stress vs. equivalent displacement for experiments conducted with the Phv apparatus using a target slip rate of 1 m/s and an acceleration of 0.5 m/s^2. c) Evolution of the axial displacement with equivalent displacement in room-dry (red) and water-dampened (blue) experiments performed with SHIVA. A positive displacement denotes compaction, a negative dilation. d) Evolution of shear stress and axial displacement (secondary y-axis) during the acceleration stage (slip rate is labeled Vel. and plotted in grey also on the secondary y-axis) to better resolve the strengthening phase, which is schematically annotated for both a room-dry (red line) and water-dampened (blue and cyan lines) experiments. The apparent large increase in compaction at the end of the water-dampened experiment is in fact an oscillation likely caused by a misalignment of the axial column; the oscillation can also be observed in the shear stress.

Figure 4: Dependence of strengthening phase and degree of weakening on the normal stress. a) Length of the strengthening phase (i.e. the slip distance to the onset of dynamic weakening) on a logarithmic

scale and b) degree of weakening in room-dry (red symbols) and water-dampened (blue and black symbols) conditions vs. the applied normal stress for experiments performed at a slip velocity of 1 m/s. Filled circles indicate experiments performed with SHIVA, diamonds indicate data from experiments performed with the Phv apparatus, which is equipped with a controlled pore-fluid pressure system. Semi-filled diamonds indicate that the gouge was pre-sheared at 1 mm/s for 30 cm. Crosses show data obtained by Smith et al. (2015) using SHIVA. Where no error bars can be seen, the error is smaller than the data points.

Figure 5: Progressive development of microstructures with displacement. Scanning electron microscope images (backscattered electrons) of room-dry (left column) and water-dampened (right column) sheared gouge samples cut tangential to the shear direction as illustrated in Fig. 2b. The sense of shear is sinistral in all images, as illustrated in a) and b). Normal stress was 8.5 MPa in all experiments. The total accumulated displacement increases from top to bottom: a) and b) 0.01 m, c) 0.13 m, d) 0.2 m, e) and f) 0.43 m, g) 1.3 m, h) 1.5 m. Image in a) was taken from Smith et al. (2015). White arrow in upper image in c) shows offset of the marker along an open R1-shear, and the red arrows in lower image point at several shear bands. White areas in d) are due to sample preparation (Pb from polishing). Lower image in d) is a higher magnification of the high-strain zone.

Figure 6: Strain distribution in the gouge layer. Quantitative strain data as obtained from measurement of the angle of distortion of the sheared marker vs. the total equivalent displacement of the respective sample. The strain was determined separately for a) the low-strain zone, b) the intermediate-strain zone and c) the high-strain zone.

Figure 7: Schematic summary of the mechanical and microstructural evolution of dry and wet calcite gouges sheared at high velocity. Phase 1) Strengthening of the gouges; development of a low-strain shear band. Phase 2) Strengthening of the dry and abrupt dynamic weakening of the wet gouges; similar microstructures marked by development of a high-strain shear band and R_1 shears. Phase 3) Both dry and wet gouges weakened to a steady-state shear stress; discrete slip surfaces within zone of heating.

9. Tables

Table 1: Experiments performed with SHIVA. Experimental conditions applied in the a) room-dry and b) water-dampened strain-marker experiments. Equivalent target slip rate was 1 m/s in all experiments.

Table 2: Experiments performed with the Phv apparatus. Experimental conditions applied in the a) room-dry and b) water-saturated experiments. Equivalent target slip rate was 1 m/s in all experiments.

Table 3: Experimental results. Length of strengthening phase ($d_{strength}$), peak and steady state shear stress (τ_{peak} and τ_{ss}, respectively) with uncertainty ranges (min. and max. values) for a) room-dry and b) wet experiments.

Table 1

	Experiment	Normal stress (MPa)	Total equivalent displacement (m)	Applied bulk strain [a]	Max. bulk strain rate (1/s) [a]	Thickness (mm) [c]	Initial thickness (mm) [e]
a) **Room-dry**	s897	3	0.29	128	441	2.14	2.27
	s886	3	2.5	1295	518	1.8	1.93
	s873	8.5	0.08	32	400	–	–
	s953	8.5	0.13	60	463	1.41	2.16[d]
	s871	8.5	0.28	112	400	–	–
	s887	8.5	0.29	109	376	2.5	2.66
	s881	8.5	0.43	195	452	2.02	2.21
	s1013	8.5	0.43	172	400	–	–
	s952	8.5	0.5	200	400	–	–
	s896	8.5	1.3	442	340	2.6	2.94
	s943	8.5	1.3	551	424	2.1	2.36
	s875	15	0.14	56	400	–	–[d]
	s889	20	0.29	141	488	1.93	2.05[d]
b) **Water-dampened[b]**	s959	8.5	0.011	6	230	1.64	1.74
	s895	8.5	0.2	80	400	–	0.9[d]
	s961	8.5	0.43	228	529	1.74	1.89
	s898	8.5	1.5	732	488	1.9	2.05
	s962	8.5	2.1	1148	546	1.55	1.83
	s279[f]	17.3	2.82	1128	400	–	–
	s389[f]	21	1.015	406	400	–	–

[a] if no initial sample thickness could be calculated, a thickness of 2.5 mm was assumed, [b] 20 wt.% distilled H_2O,
[c] thickness of sheared gouge layer evaluated from the SEM pictures, [d] material loss during sample preservation,
[e] obtained from [c] and the amount of compaction measured during the experiment [f] no strain marker

Table 2

		Experiment	Normal stress (MPa)	Fluid pressure (MPa)	Total equivalent displacement (m)	Pre-sheared?
a)	**Room-dry**	phv311	3	-	5.5	Y
		phv343	3	-	3.72	N
		phv299	8.5	-	15.62	Y
		phv301	8.5	-	17.62	Y
b)	**Water-saturated**	phv305	1	1.5	18.42	Y
		phv306	1	0.2	19.22	Y
		phv290	3	7	22.00	Y
		phv304	3	1.5	19.12	Y
		phv310	3	0.6	5.31	Y
		phv313	3	0.6	5.32	N
		phv337	3	7	4.86	Y
		phv347	3	7	3.88	N
		phv355	3	7	2.18	Y
		phv340	4	6	4.92	Y
		phv351	4.5	10.5	4.03	Y
		phv350	6	9	4.25	Y
		phv291	8.5	1.5	22.70	Y
		phv292	8.5	1.5	16.06	Y
		phv297	8.5	1.5	18.40	Y
		phv298	8.5	1.5	17.43	Y
		phv300	8.5	1.5	9.91	Y
		phv312	8.5	1.5	5.12	Y
		phv307	10	2	4.82	Y
		phv309	12	1.5	12.82	Y

Table 3

		Experiment	$d_{strength}$ (m)	$d_{strength,min}$ (m)	$d_{strength,max}$ (m)	τ_{peak} (MPa)	$\tau_{peak,min}$ (MPa)	$\tau_{peak,max}$ (MPa)	τ_{ss} (MPa)	$\tau_{ss,min}$ (MPa)	$\tau_{ss,max}$ (MPa)
a)	Room-dry	s897	-	-	-	1.51	1.24	1.77	-	-	-
		s886	0.78	0.48	0.80	2.29	2.15	2.39	1.44	1.20	1.57
		s953	-	-	-	5.14	5.05	5.23	-	-	-
		s871	0.09	0.09	0.10	4.79	4.64	4.93	4.20	3.39	4.32
		s887	0.11	0.08	0.12	5.58	5.17	5.67	-	-	-
		s881	0.09	0.06	0.09	5.27	4.74	5.32	3.06	2.43	3.70
		s1013	0.10	0.10	0.11	5.79	5.61	5.84	3.18	2.90	3.47
		s952	0.19	0.18	0.23	5.64	5.46	5.82	2.63	2.26	3.00
		s896	0.10	0.06	0.11	5.24	4.47	5.42	3.32	2.17	4.47
		s943	0.11	0.11	0.12	5.45	5.24	5.56	2.88	2.37	3.40
		s875	0.08	0.05	0.08	11.27	11.00	11.53	-	-	-
		s889	0.03	0.03	0.04	14.50	14.31	14.68	5.38	4.84	5.91
		phv299	0.13	0.13	0.13	7.79	7.74	7.84	1.79	1.67	2.16
		phv301	0.15	0.14	0.15	7.85	7.77	7.89	1.54	1.12	2.07
		phv311	0.56	0.33	0.58	2.59	2.24	2.60	1.28	1.18	1.39
		phv343 [a]	0.29	0.28	0.40	2.79	2.64	2.82	1.57	1.44	1.70
b)	Water-dampened/-saturated	s959	0.0055	0.0013	0.0060	4.81	4.47	5.36	-	-	-
		s895	0.0015	0.0010	0.0043	4.62	4.37	4.96	3.69	3.53	3.92
		s961	0.0082	0.0038	0.0530	4.71	4.62	4.85	3.70	3.30	4.15
		s898	0.0030	0.0023	0.0638	4.87	4.53	5.39	3.77	3.32	4.21
		s962	0.0052	0.0014	0.0085	4.75	4.45	5.30	3.86	3.54	4.18
		s279	0.0058	0.0043	0.0074	11.49	10.94	11.69	4.36	3.70	5.02
		s389	0.0423	0.0378	0.0569	11.72	5.38	18.07	4.20	3.14	5.27
		phv291	0.0021	0.0017	0.0023	5.86	5.38	6.34	1.79	1.55	2.03
		phv292	0.0011	0.0006	0.0013	5.29	5.38	5.20	1.34	1.22	1.46
		phv297	0.0011	0.0011	0.0324	5.51	5.38	5.65	1.43	1.14	1.71
		phv298	0.0014	0.0013	0.0507	5.79	5.38	6.20	2.36	2.05	2.67
		phv300	0.0008	0.0006	0.0676	5.78	5.38	6.18	3.00	2.84	3.17
		phv312	0.0009	0.0007	0.0012	5.76	5.38	6.14	1.79	1.55	2.02
		phv306	0.0080	0.0066	0.0574	3.22	5.38	1.06	0.52	0.42	0.61
		phv310	0.0011	0.0009	0.0015	3.94	5.38	2.51	1.14	0.95	1.33
		phv307	0.0008	0.0007	0.0008	6.06	5.38	6.75	2.17	1.95	2.38
		phv309	0.0006	0.0006	0.0008	7.05	5.38	8.72	2.23	1.90	2.56
		phv304	0.0046	0.0035	0.0048	3.90	5.38	2.42	1.11	0.99	1.24
		phv305	0.0136	0.0130	0.0141	3.15	5.38	0.91	0.36	0.29	0.44
		phv340	0.0038	0.0036	0.0040	3.76	5.38	2.14	0.90	0.67	1.24
		phv350	0.0036	0.0036	0.0046	3.92	5.38	2.45	1.41	0.96	1.87
		phv290	0.0077	0.0077	0.0120	3.47	5.38	1.57	0.69	0.65	0.73
		phv337	0.0130	0.0109	0.0154	3.36	5.38	1.35	0.66	0.50	0.83
		phv355	0.0346	0.0047	0.0346	3.29	5.38	1.20	0.28	0.25	0.31
		phv351	0.0139	0.0038	0.0144	3.50	5.38	1.61	0.47	0.42	0.52
		phv313 [a]	0.0066	0.0060	0.1754	3.86	5.38	2.34	1.31	1.12	1.50
		phv347 [a]	0.0007	0.0006	0.0048	3.22	5.38	1.06	0.13	0.10	0.24

[a] Phv-experiments without pre-shearing

Figure 1

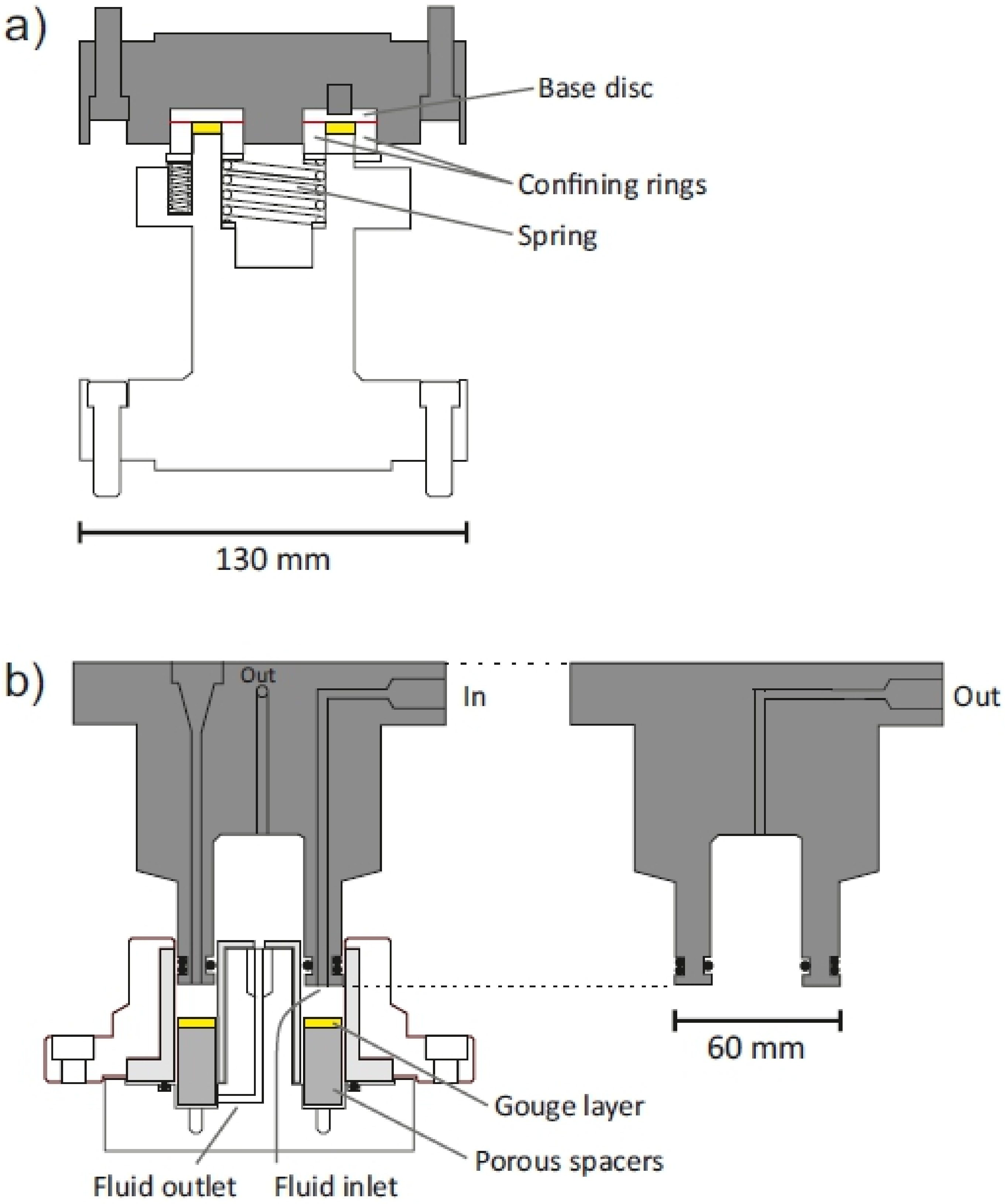
a)
Base disc
Confining rings
Spring
130 mm
b)
Out
In
Out
60 mm
Gouge layer
Porous spacers
Fluid outlet
Fluid inlet

Figure 2

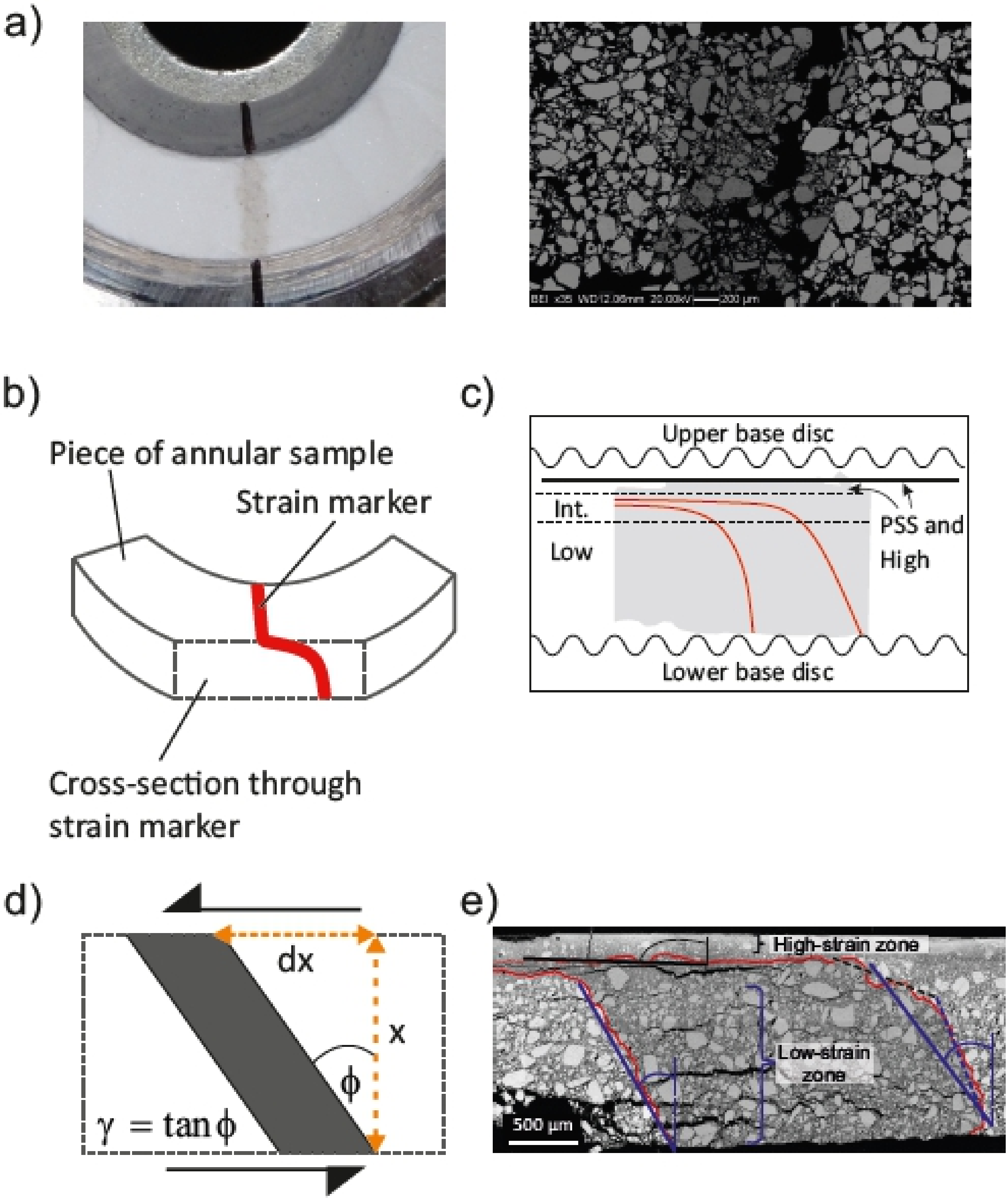
a)
BEI x35 WD12.06mm 20.00kV 200 µm
b)
Piece of annular sample
Strain marker
Cross-section through strain marker
c)
Upper base disc
Int.
Low
PSS and High
Lower base disc
d)
dx
x
ϕ
γ = tan ϕ
e)
High-strain zone
Low-strain zone
500 µm

Figure 3

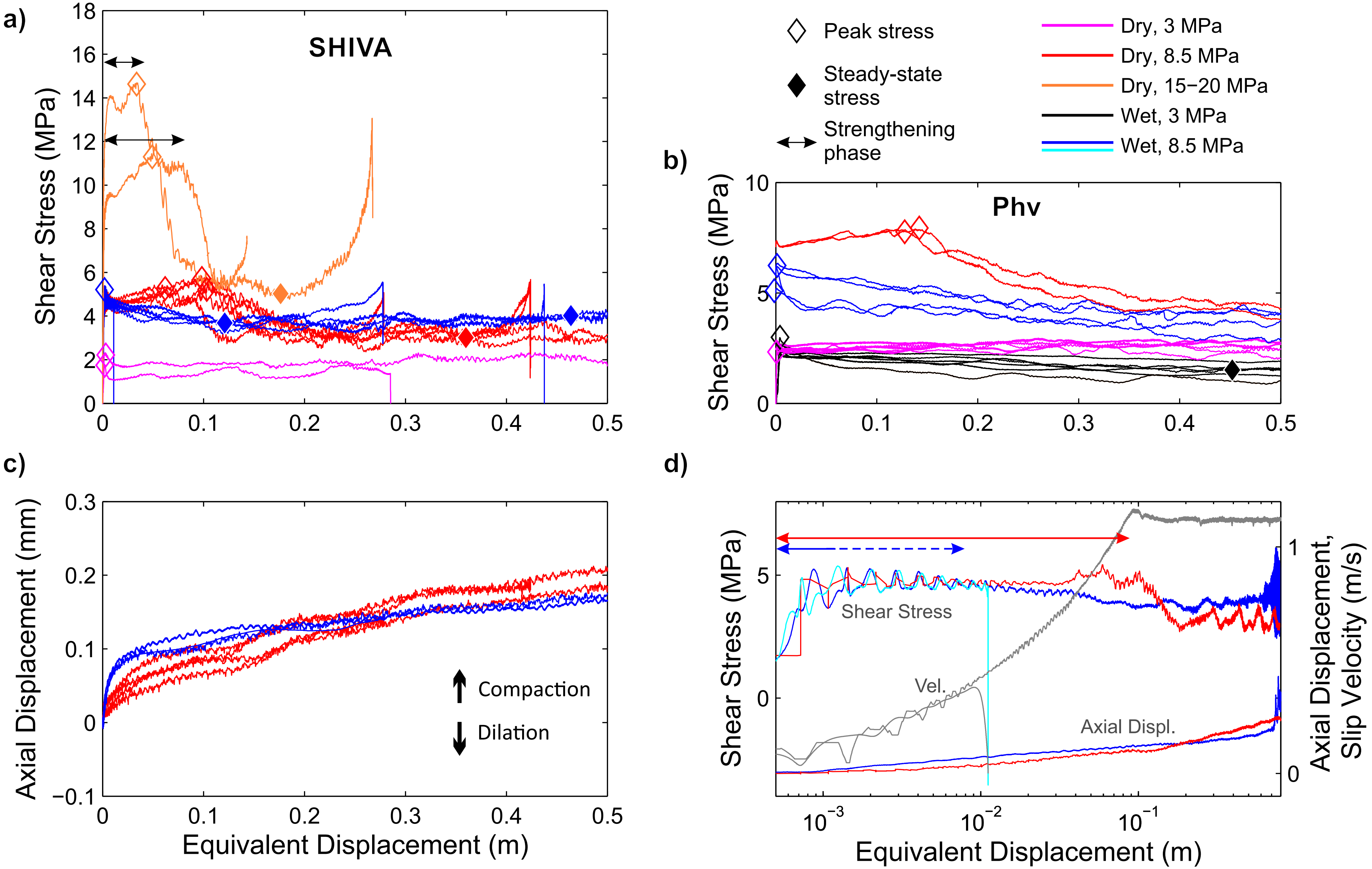
a)
SHIVA
Shear Stress (MPa)
18
16
14
12
10
8
6
4
2
0
0
0.1
0.2
0.3
0.4
0.5
◇ Peak stress
◆ Steady-state stress
↔ Strengthening phase
Dry, 3 MPa
Dry, 8.5 MPa
Dry, 15−20 MPa
Wet, 3 MPa
Wet, 8.5 MPa
b)
Phv
Shear Stress (MPa)
10
5
0
0
0.1
0.2
0.3
0.4
0.5
c)
Axial Displacement (mm)
0.3
0.2
0.1
0
−0.1
0
0.1
0.2
0.3
0.4
0.5
Equivalent Displacement (m)
Compaction
Dilation
d)
Shear Stress (MPa)
5
0
Shear Stress
Vel.
Axial Displ.
Axial Displacement, Slip Velocity (m/s)
1
0
10^−3
10^−2
10^−1
Equivalent Displacement (m)

Figure 4

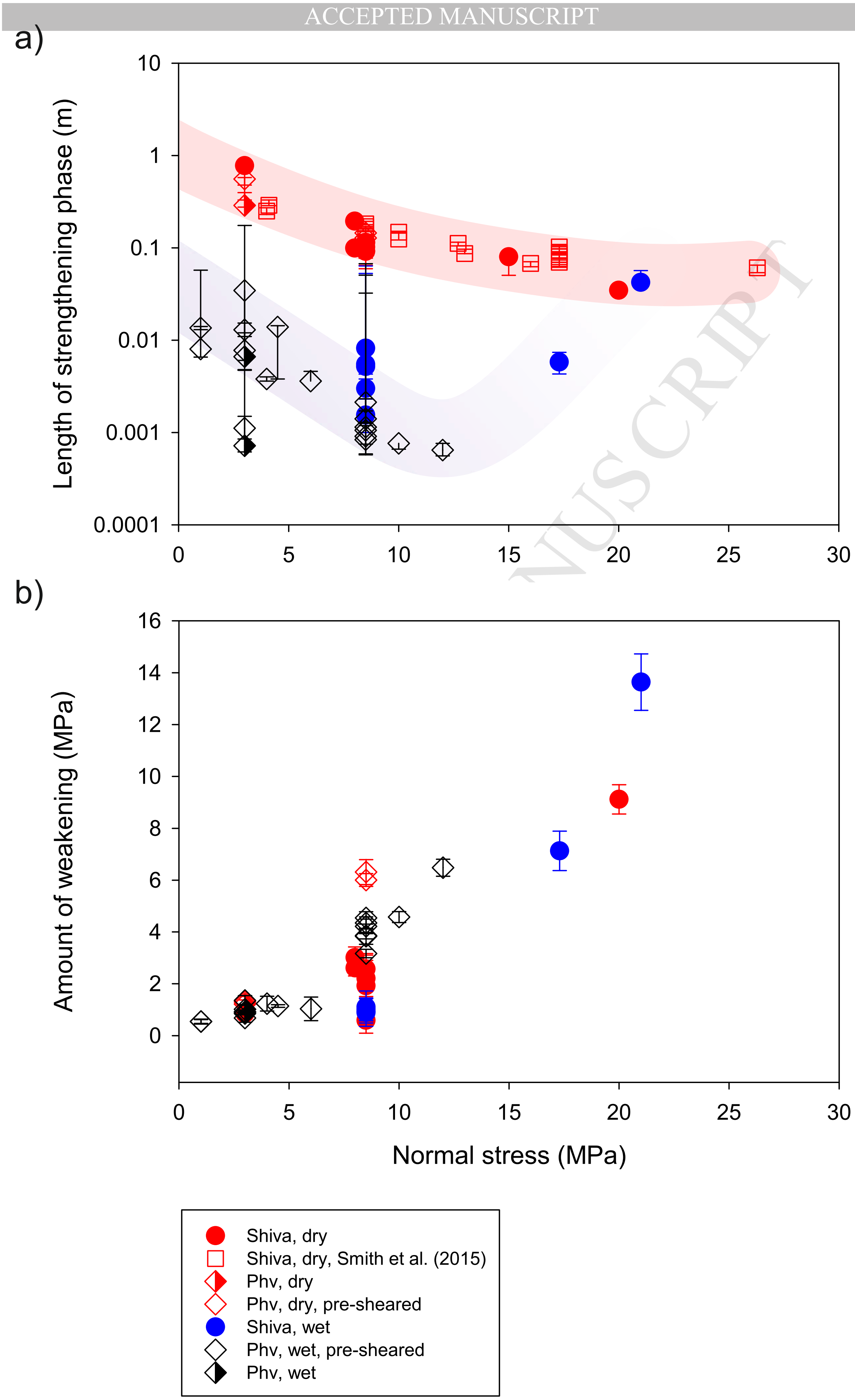
a)
Length of strengthening phase (m)
10
1
0.1
0.01
0.001
0.0001
0
5
10
15
20
25
30
b)
Amount of weakening (MPa)
16
14
12
10
8
6
4
2
0
0
5
10
15
20
25
30
Normal stress (MPa)
● Shiva, dry
□ Shiva, dry, Smith et al. (2015)
◆ Phv, dry
◇ Phv, dry, pre-sheared
● Shiva, wet
◇ Phv, wet, pre-sheared
◆ Phv, wet

Figure 5

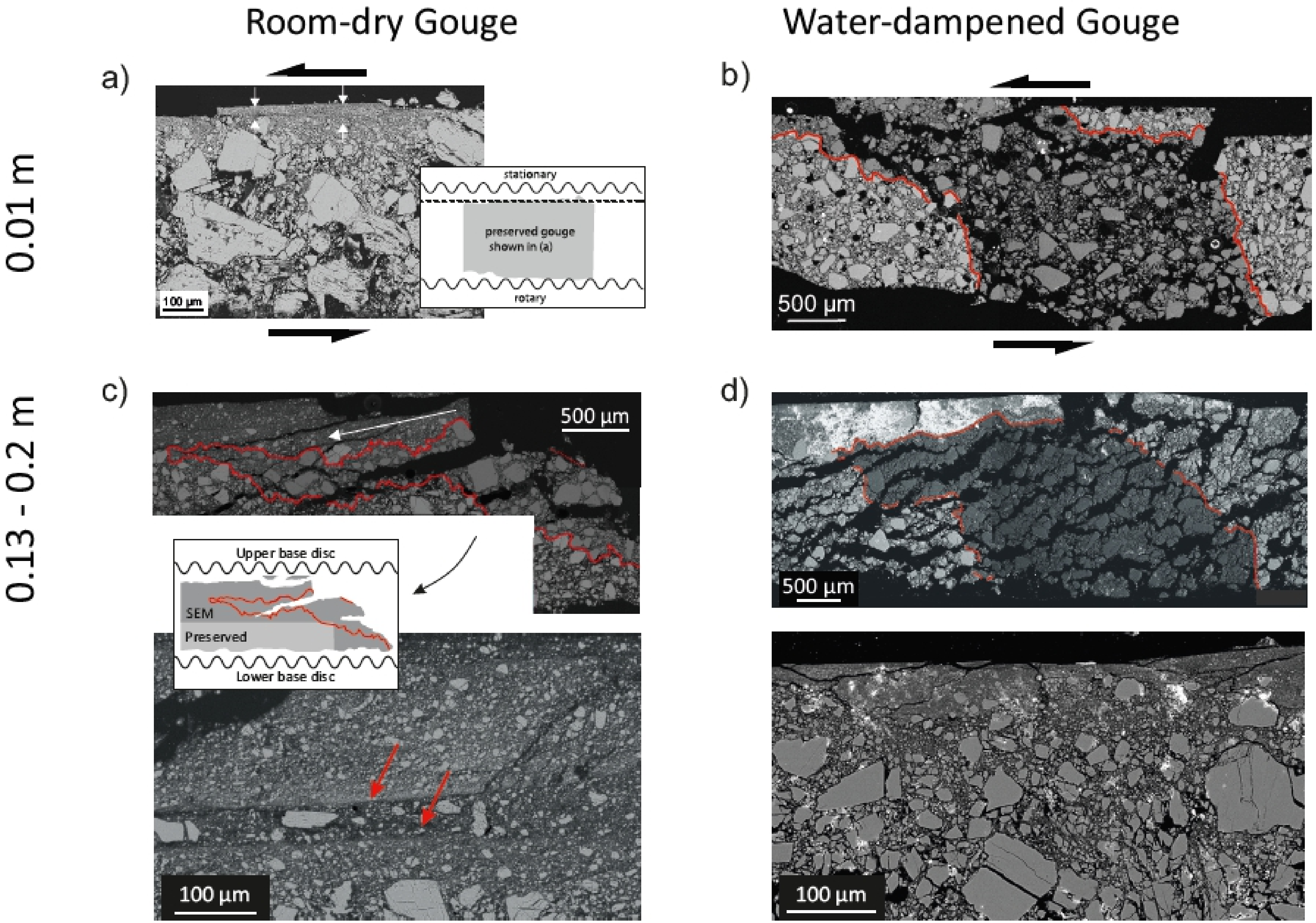
Room-dry Gouge
Water-dampened Gouge
0.01 m
0.13 - 0.2 m
a)
100 µm
stationary
preserved gouge shown in (a)
rotary
b)
500 µm
c)
500 µm
Upper base disc
SEM
Preserved
Lower base disc
100 µm
d)
500 µm
100 µm

Figure 5 continued

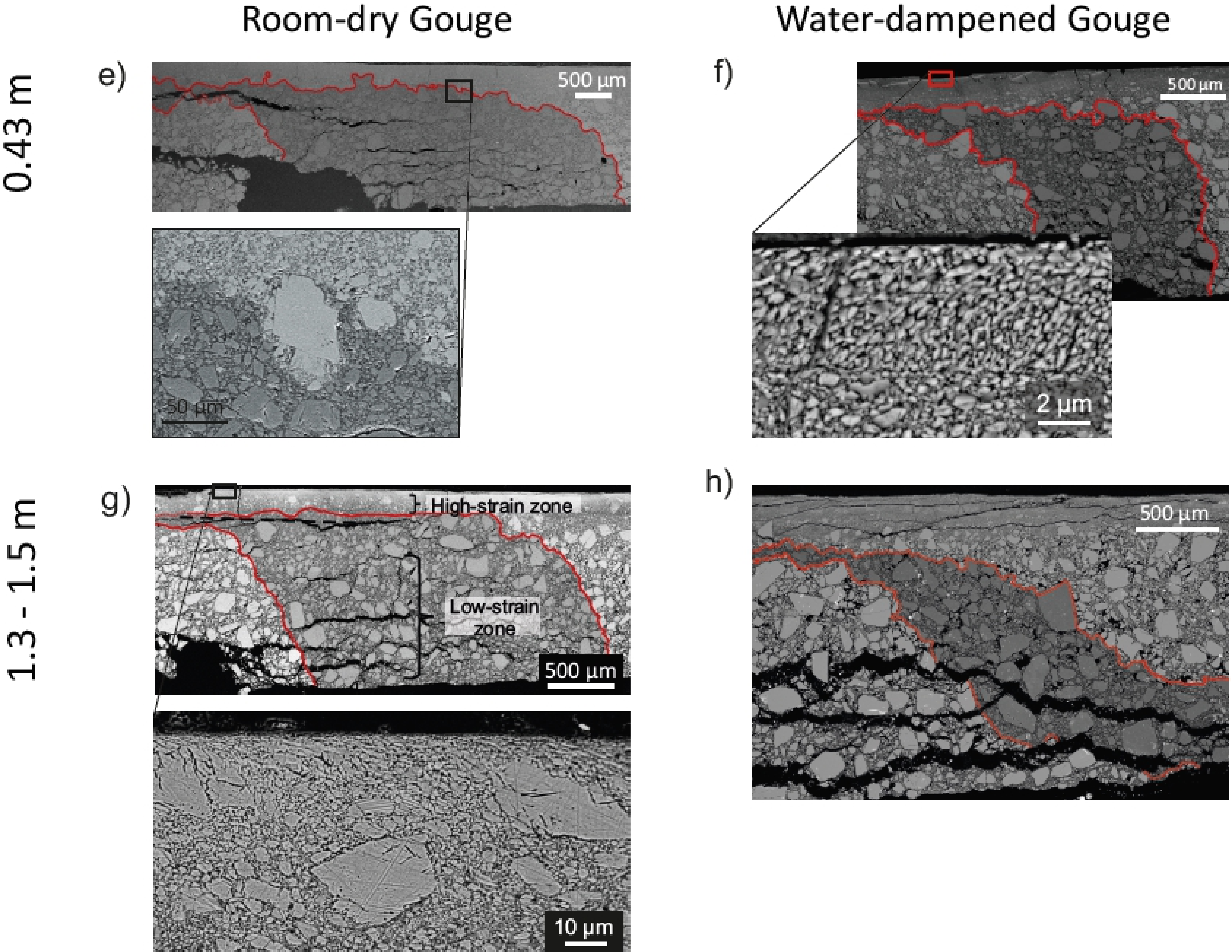

Figure 6

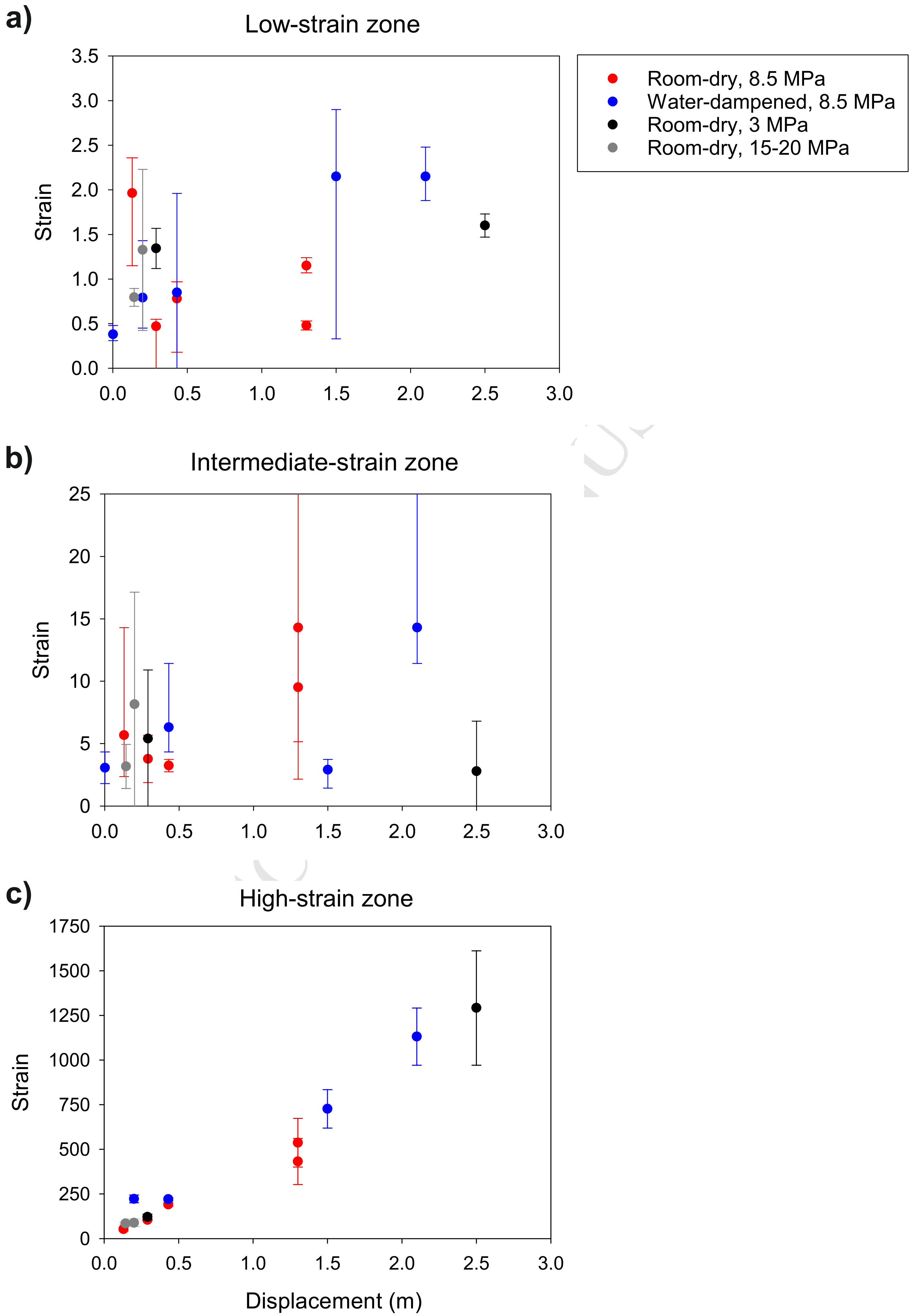
a)
Low-strain zone
Strain
3.5
3.0
2.5
2.0
1.5
1.0
0.5
0.0
0.0
0.5
1.0
1.5
2.0
2.5
3.0
● Room-dry, 8.5 MPa
● Water-dampened, 8.5 MPa
● Room-dry, 3 MPa
● Room-dry, 15-20 MPa
b)
Intermediate-strain zone
Strain
25
20
15
10
5
0
c)
High-strain zone
Strain
1750
1500
1250
1000
750
500
250
0
Displacement (m)

Figure 7

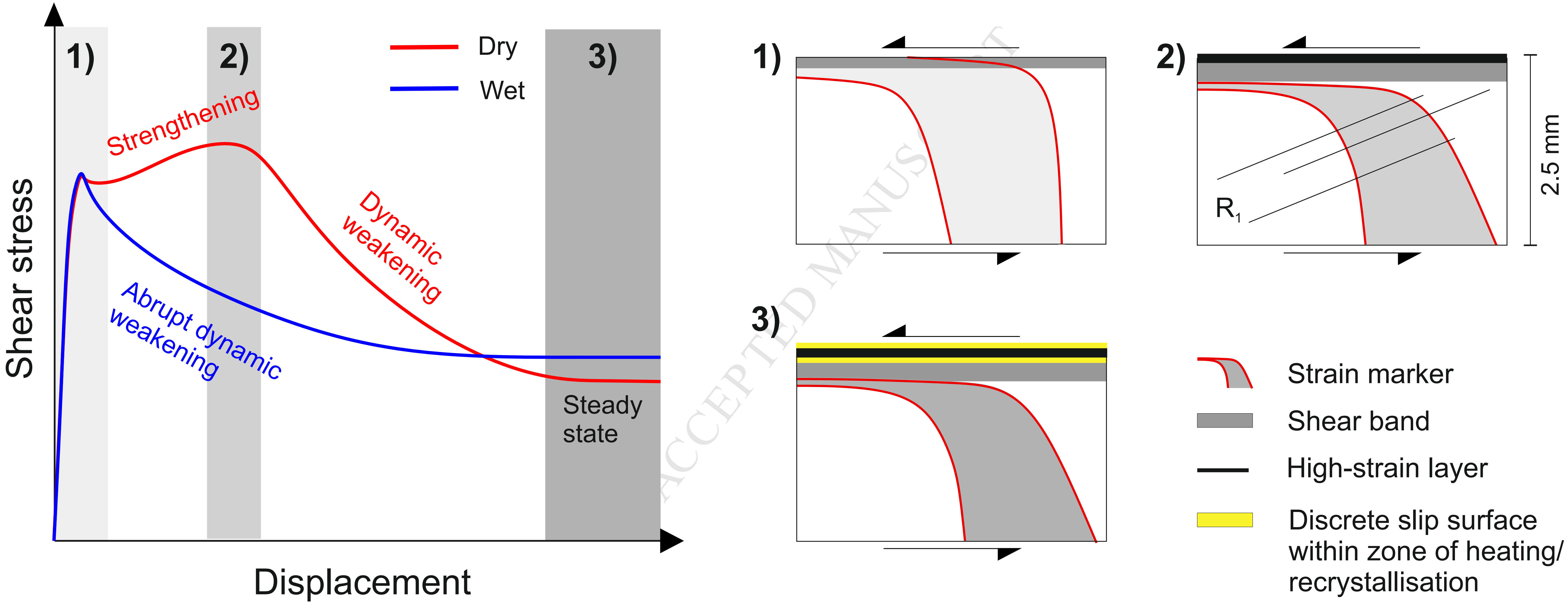
Shear stress
Displacement
1)
2)
3)
Dry
Wet
Strengthening
Dynamic weakening
Abrupt dynamic weakening
Steady state
1)
2)
3)
R1
2.5 mm
Strain marker
Shear band
High-strain layer
Discrete slip surface within zone of heating/ recrystallisation

Highlights

1) High-velocity, rotary-shear experiments on dry and wet calcite gouges

2) Strain localization during shear occurs progressively and rapidly

3) Dynamic weakening in calcite gouges is accelerated in the presence of fluids

4) In wet gouges, strain localization does not occur prior to dynamic weakening

5) Carbonate-bearing faults are more prone to slip in the presence of water